Engineering Science & Technology
https://ojs.wiserpub.com/index.php/EST/

UNIVERSAL WISER PUBLISHER

Research Article

Thermomechanical Modeling and Fabrication of Structurally Reinforced Soft Pulse Separation Devices for Dual-Pulse Motors

Jacob Nagler

Nagler Independent Research Center, NIRC, Haifa, Givat Downs, 34345, Israel
E-mail: jacobyan123@gmail.com

Received: 30 April 2026; **Revised:** 29 May 2026; **Accepted:** 10 June 2026

Abstract: The Structurally Reinforced Soft Pulse Separation Device (SPSD) is a pivotal technology for enabling flexible energy management in Dual-Pulse Solid Rocket Motors (DP-SRMs), yielding significant mass savings and nozzle safety advantages over rigid bulkheads. However, predicting the stochastic rupture behavior of elastomeric membranes under combined thermal and pneumatic loads remains a primary design challenge. This paper proposes a unified Thermomechanical Membrane Rupture Model (TMRM) that integrates Pulse-I thermal ablation history with Pulse-II large-deformation kinematics. Addressing critical gaps in contemporary literature, the model explicitly delineates the phenomenological transition between linear plate theory (applicable to rigid metallic barriers) and non-linear secant-modulus Hencky approximations (essential for soft elastomers). Validated against high-fidelity Fluid-Structure Interaction (FSI) simulations and experimental datasets, the results demonstrate that reliance on classical linear theory for elastomers severely underestimates pressure capacity. Large-deformation geometric stiffening allows Ethylene Propylene Diene Monomer (EPDM) membranes to withstand pressures up to ~ 80% higher than linear predictions. Furthermore, a counter-intuitive thermal hardening phenomenon is quantified, wherein ablation-induced thinning of the bulk membrane paradoxically increases structural compliance, relaxes the radius of curvature, and elevates the rupture threshold, thereby maintaining a robust safety margin during the coast phase. By bridging the gap between elastomeric material science and internal ballistics, this analytic framework establishes a deterministic preliminary sizing protocol for reliable, low-fragmentation petaling in next-generation tactical propulsion systems.

***Keywords*:** Dual-Pulse Solid Rocket Motor (DP-SRM), Pulse Separation Device (PSD), thermomechanical rupture model, large-deformation kinematics, Fluid-Structure Interaction (FSI), thermal hardening

Nomenclature

a, n	Propellant-specific ablation power-law constants
E_{sec}	Secant modulus of the composite membrane (MPa)
h_0	Initial bulk thickness of the Soft Pulse Separation Device (SPSD) (mm)
h_{char}	Depth of the pyrolyzed char layer (mm)
h_{eff}	Residual structural effective thickness (mm)
h_{groove}	Thickness at the root of the pre-scored groove (mm)
K_1, K_2	Dimensionless Hencky constants dependent on Poisson's ratio ($\nu \approx 0.5$)

DOI: https://doi.org/10.37256/est.72202610095

P_I, P_{II}	Pressure of Pulse I and Pulse II phases respectively (MPa)
P_{burst}	Critical Pulse II ignition pressure required to rupture the SPSD (MPa)
R	Internal radius of the clamped SPSD port (mm)
r	Ablation rate of the SPSD insulation material (mm/s)
V_f	Volume fraction of reinforcing fibers
w_0	Center (pole) deflection of the membrane (mm)
A	Empirical stress concentration shape factor of the groove notch
$\beta(r)$	Radial stress decay distribution factor
σ_{local}	Local amplified stress at the groove root (MPa)
σ_{pole}	Peak radial stress at the center pole of the membrane (MPa)
σ_{UTS}	Ultimate tensile strength of the composite material (MPa)

1. Introduction

The Dual-Pulse Solid Rocket Motor (DP-SRM) represents a paradigm shift in tactical missile propulsion, introducing energy management capabilities previously exclusive to liquid propulsion. By segregating the propellant into two distinct pulses via a Pulse Separation Device (PSD), the motor facilitates distinct ignition, coast and re-ignition phases.

The reliability of the DP-SRM is intrinsically linked to the PSD. Early architectures utilized “hard” rigid bulkheads composed of ceramics or metallic alloys [1], [2]. While it is possible to design metallic barriers without ejecting fragments [2], rigid bulkheads generally introduce significant parasitic mass and presents the risk of ejecting high-density debris that threatens nozzle throat integrity. Consequently, recent research has pivoted toward Structurally Reinforced “Soft” Pulse Separation Devices (SPSDs); these are flexible diaphragms offering reduced inert mass and minimized risk of nozzle damage, typically constructed from fabric-reinforced elastomers [3], [4].

Despite their advantages, SPSDs present complex aerothermal challenges. The device must function as a robust thermal insulator protecting the Pulse-2 grain during the first pulse (Pulse I), and transition to a frangible membrane during the ignition of the second pulse (Pulse II). The time needed to rupture the SPSD directly affects the start of thrust and pressure transients. This paper reviews the state-of-the-art in SPSD mechanics and proposes a unified analytic design framework, the Thermomechanical Membrane Rupture Model (TMRM), providing an engineering bridge between computationally expensive Fluid-Structure Interaction (FSI) simulations and oversimplified linear theory.

1.1 *Literature review: boundary conditions and transition to soft barriers*

1.1.1 *Limitations of rigid vs. soft barriers*

Rigid barriers (e.g., metallic or ceramic domes) often rely on sliding ports, reverse-buckling mechanisms, or shockwave-induced shattering. The feasibility of utilizing such rigid bulkheads has been demonstrated in early programs as well as in more recent studies [5]. Stadler et al. [1] describe the design of a fragment-free rigid PSD. Implemented in the Lenkflugkörper Neue Generation (“New Generation Guided Missile”) (LFK-NG) program, this configuration utilized a rigid metallic bulkhead designed to open cleanly without shedding debris, achieving an isostatic barrier function [6], [7]. Nevertheless, literature indicates a critical failure mode of incomplete fragmentation, where large shards cause nozzle throat erosion or blockage. Additionally, rigid barriers require fixed geometric clearances, limiting the volumetric loading of the Pulse I propellant. In contrast, a true “soft” PSD relies on elastomeric compliance, acting as a flexible protective cover that stretches and tears rather than shatters. State-of-the-art architectures frequently utilize a hybrid: a rigid outer support ring clamped to the motor case and a soft reinforced elastomeric core spanning the port [3]. The time required to rupture the SPSD directly affects the start of thrust and pressure transients.

SPSDs, typically based on Ethylene Propylene Diene Monomer (EPDM) reinforced with Aramid or Kevlar fibers, resolve these issues: (i) Mass efficiency: EPDM-based composites (density < 1.2 g·cm^{-3}) have a much lower inert mass than ceramic materials (density > 2.5 g·cm^{-3}). (ii) Nozzle safety: Soft debris (rubber or fabric) is deformable and passes through nozzles with negligible erosive wear, an important advantage for modern, intricate nozzle geometries. (iii) Volume efficiency: As [4] shows, soft barrier designs that bulge under pressure can increase the propellant loading fraction.

1.1.2 *FSI dynamics*

The opening dynamics of soft SPSDs are governed by strong Fluid-Structure Interaction (FSI). Unlike rigid bulkheads (i.e. barriers) that shatter instantaneously, soft barriers undergo significant large-strain deformation (bulging) prior to ultimate tensile failure [8], [9]. This deformation acts as an accumulator, dampening the ignition shockwave. Consequently, predicting the rupture threshold cannot be achieved through classical small-deflection plate theory.

1.1.3 *Structural layout and clamped boundary idealization*

Modern SPSDs typically feature a multi-layered composite layup (sandwich structural configuration) to meet conflicting thermal and mechanical requirements. The SPSD layer-wise material configuration typically comprises an external ablative layer (Pulse-1-facing side), an internal load-bearing fabric (e.g., Kevlar-reinforced EPDM), and an initiation layer (Pulse-2-facing side). However, to analytically model the underlying mechanics of this system, the device is first idealized as a circular membrane subjected to a perfectly clamped boundary condition at the radius R. To avoid conceptual redundancy with the practical engineering layups presented later, Figure 1 is dedicated strictly to the theoretical topology and kinematics of the deformation. Practically, this assumption is justified when the outer metallic support frame is laser-welded or heavily bolted to the motor case, preventing radial slippage. Any deviation from a perfect clamp (e.g., adhesive shear creep) would increase edge compliance, rendering the analytical predictions conservative. This schematic depicts the idealized boundary conditions, the abstract spatial arrangement of pre-scored weakness lines, and the geometric transition of a flat disk stretching into a spherical-cap bulge under uniform pressure. This abstraction provides the coordinate system and geometric assumptions necessary to derive the closed-form Hencky equations in Section III, entirely separate from physical material layering and case-bonding details.

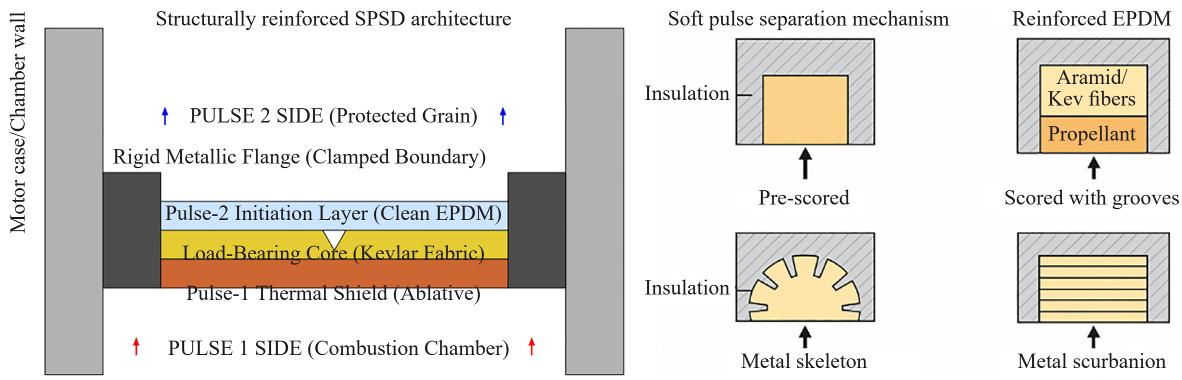

Figure 1. Schematic configuration solutions of SPSDs

Contemporary literature converges on the conclusion that material choice and structural layout are the fulcrum upon which the performance and safety of Soft Pulse Separation Devices (SPSDs) pivot. At the heart of the design tension is a bifunctional requirement: during the initial burn, the separation device must behave as an effective thermal and mechanical insulator, preserving the integrity of the second grain, while during the second ignition, it must transition cleanly and predictably to a fragile membrane that opens without producing hazardous, nozzle-damaging fragments. Reconciling these contradictory demands has driven the field toward hybrid material systems and carefully controlled structural architectures rather than monolithic solutions.

Ethylene Propylene Diene Monomer (EPDM) emerges repeatedly in peer-reviewed work as the reference matrix for soft barriers, prized for its favorable density, oxidation and aging resistance, and capacity to form char layers under thermal load that afford a degree of ablative protection [4], [10], [11]. Nevertheless, the consensus is nuanced: unreinforced EPDM lacks sufficient stiffness to survive the pressure differential and mechanical loading of the first pulse without excessive deformation or rupture, while heavily reinforced rubbers lose the membrane's necessary ductility and fail to open reliably during the second pulse. To navigate this compromise, researchers have concentrated on composite EPDM formulations in which aramid or Kevlar fiber phases provide load-bearing structure while the elastomeric phase supplies compliance and ablation resistance. The balance between reinforcement density, fiber orientation, and matrix toughness is therefore the primary material design variable.

Structurally, the dominant architectural motif in modern SPSD research is the sandwich or layered composite: an external thermal insulation layer facing the first pulse, an internal load-bearing fabric or skeleton, and a secondary insulation facing the second pulse. This topology decouples the thermal-protection and mechanical-rupture functions, permitting each layer to be tuned independently. Within this paradigm, geometric features intended to localize strain pre-scored grooves [12], stress concentrators, or engineered weakness lines, are widely reported as effective means to drive repeatable splitting behavior. When properly executed, these pre-scores promote a petal-like opening that fragments the soft barrier into compliant pieces rather than long strips or intact sections that could snag in the nozzle. The weave pattern and orientation of the reinforcing fabric (for example, radial versus plain weave) prove determinative of rupture paths: the fabric controls how and where the membrane concentrates deformation energy and thus whether the failure progresses as an orderly tear or an uncontrolled tear that produces unwanted debris [3], [13].

The dynamic process by which the barrier transitions from an effective seal to debris, commonly termed the "opening moment", is the most technically challenging phenomenon to predict and to control. Unlike brittle, hard barriers that shatter almost instantaneously, soft barriers undergo substantial large-strain deformation: the inner face bulges under the pressure impulse of the pulse-two igniter, stretches, and eventually tears. This sequence is sensitive to the barrier's opening pressure threshold: if the threshold is set too low, the membrane may yield during the coast phase through thermal softening or gradual mechanical creep and compromise the second grain; if set too high, the system accumulates excess pressurization during ignition, risking an overpressure event in the downstream chamber or damage to the motor case. Experimental work using high-speed imaging, coupled with hydrocode diagnostics, consistently documents this pre-rupture bulging behavior and highlights the narrow window of acceptable opening thresholds [3], [12], [14].

Modeling the opening dynamics requires capturing a two-way interaction between fluid transients and structural response; conventional, single-domain Computational Fluid Dynamics (CFD) approaches are inadequate because the geometry, boundary conditions, and material state evolve dramatically within milliseconds. Consequently, state-of-the-art studies use coupled multi-physics strategies, Coupled Eulerian-Lagrangian (CEL) formulations, Smoothed Particle Hydrodynamics (SPH), and other two-way Fluid-Structure Interaction (FSI) schemes to represent both the continuum deformation of the membrane and the transient gas dynamics. These approaches reveal that the large deformation of soft barriers acts to absorb and attenuate the initial shock, reducing peak impulse and "water hammer" transmission to the nozzle compared with hard barriers; still, accurate predictions demand careful representation of the material's evolving constitutive behavior, including thermal softening, char formation, and potential delamination at bonded interfaces [5], [9], [14].

Thermal-structural reliability during the first burn remains a central design constraint. As the SPSD faces radiative and convective heating, EPDM and related elastomers undergo surface pyrolysis and charring; this creates a thermal-protective layer although simultaneously alters mechanical properties. If the pyrolysis penetrates too deeply, the residual structure becomes charred and brittle, increasing the risk of fragmentation during coast and unintended failure prior to the intended opening event. Conversely, insufficient char means the membrane remains too ductile and may not rupture cleanly when pressurized. Predictive models therefore focus on pyrolysis depth and residual thickness following Pulse I [12], and experimental programs emphasize post-fire sectioning to verify the char profile [11], [15]. Another practical challenge documented across multiple studies is slag accumulation, principally alumina (Al_2O_3), from combustion by-products. Slag deposition increases the local thermal load, adds static mass to the barrier, and can introduce sag under high acceleration loading, all of which perturb both the mechanical pre-stresses and the effective internal volume. The net effect can be deleterious to the planned opening dynamics, particularly where bonding interfaces are mechanically marginal.

When the barrier ruptures, the downstream interaction between expelled debris and the nozzle is a decisive safety and performance consideration. Comparative post-fire analyses and throat inspection studies show that compliant rubber and fabric fragments are markedly less erosive than ceramic or metallic shards; soft debris tends to deform and pass through converging geometry with lower material removal rates and less gouging of the throat. Nevertheless, the literature flags a nontrivial risk that long, contiguous strips of soft insulation can temporarily catch on the convergence, producing transient thrust asymmetries. To mitigate this, contemporary research explores frangible rubber formulations and engineered fracture paths designed to produce smaller particulate debris rather than intact ribbons.

Against this backdrop, soft SPSDs are increasingly portrayed as the preferred choice for tactical, high-performance dual-pulse solid rocket motors because they address two primary constraints: they materially reduce inert mass compared to rigid ceramic bulkheads, thereby improving mass fraction and performance, and they minimize erosive risk to modern vectoring nozzles, whose complex geometries and moving components are intolerant of hard fragments. Active, pyrotechnic, and frangible ceramic approaches retain advantages in contexts where hermetic sealing, extreme long-term storage, or insensitivity to fragment debris are paramount; for example, in large strategic boosters or systems requiring decades of storage reliability, still, for many operational profiles the soft, pre-scored SPSD represents the optimum compromise.

1.1.4 *Thermal protection, controlled-rupture design, bonding, and validation for Pulse-1 soft PSDs*

Thermal protection for the Pulse-1 face of soft PSDs is generally required but conditional: the need and form of protection depend on diaphragm material, Pulse-1 temperature/time history, and the ability of the barrier system to survive mechanical loads while limiting thermal penetration. Past practice (e.g., the LFK-NG concept [1], [7]) sandwiches the diaphragm behind an insulating backing (Kevlar-filled EPDM, phenolic/silica laminates) to prevent burn-through and limit diaphragm heating; where hot-gas exposure to structural supports is severe, thermal-barrier coatings (TBCs, [16], [17]) on the support (not on the sacrificial diaphragm) are a practical option provided adhesion and mechanical survivability are demonstrated. In short: metal-foil diaphragms should be backed by insulation (silica/phenolic or Kevlar/EPDM) and may receive thin bonding coats on the support, whereas polymer diaphragms (e.g., Kapton HN [18]) must be kept out of direct flame or used only for short Pulse-1 durations with robust insulation because polymers de-rate rapidly with temperature.

Controlled rupture via scoring (ring grooves, radial scribe lines or cruciform patterns) is an established method to lower and homogenize burst pressure and to encourage clean petalling rather than fragmentation. Reverse-buckling discs are another controlled-burst design used widely [19]. Groove depth and pattern reduce the effective cross-section and concentrate strain along intended tear lines, producing repeatable opening when the groove geometry and manufacturing tolerances are tightly controlled; however, designers must account for rate effects because dynamic loading (ignition transients) [12], [20] can raise burst pressure relative to static tests. Recommendation: target burst pressure with shallow ring-grooves or radial scribe lines, then validate the chosen pattern across the expected temperature and pressurization-rate envelope.

Adhesive strategy and interface design are critical to prevent premature PSD failure during Pulse-1 and to ensure the bond survives cure and aging [21]. The preferred approach is case-bonding (see [22]), casting propellant against a cured, surface-treated liner so the propellant chemically bonds into the liner [23], [24]; because this eliminates weak adhesive interlayers; where direct casting is impractical, use flexible adhesives or bond promoters (such as aziridine-type Tris(Methyl-Aziridinyl) Phosphine Oxide/Trimesoyl-1-(2-ethylaziridine) (MAPO/BITA) as appear in [23], or primers evaluated in [25]) to improve Hydroxyl-Terminated Polybutadiene (HTPB)/liner adhesion [26]. Mechanically preload the diaphragm with a clamped ring and gasket so transient peel/tensile loads are carried by the clamp rather than the adhesive; avoid directly gluing thin metal diaphragms to propellant unless the bond chemistry and cure have been fully validated [5]. Remark that the historical patents [8] and adhesively bonded engines cited [21] use flexible resin adhesives and direct casting methods.

A concise test and validation matrix is mandatory (see Appendix): (i) component static burst tests (hydro) at room and elevated temperatures in both orientations (pressurize Pulse-1 side and conversely pressurize Pulse-2 side to measure burst); (ii) dynamic full-motor static firings [7] to confirm opening behavior and that any fragments do not damage downstream hardware; and (iii) scored-sample tests [20] that quantify static versus dynamic burst pressures across multiple groove depths and temperatures (expect dynamic burst to be occasionally higher). These steps bridge analytic design and FSI realities and are required before any flight application.

Finally, a practical, literature-backed bonding workflow and shop-floor tips condense to the following baseline: surface preparation (solvent clean, light abrasion or grit-blast as appropriate), thin primer/bond-promoter coat with controlled dwell (MAPO/BITA or Isophorone Diisocyanate (IPDI) per supplier guidance), mechanical clamping of the diaphragm with a thin gasket and cross-torqued ring, installation of a fully cured/primed liner, careful propellant casting against the liner case-bond [22], [27], full cure and prescribed post-cure, then visual/Non-Destructive Testing (NDT) inspection and coupon pull/peel tests [21], [25].

A summary with sample typical Trade-offs appears in Table 1 alongside the following comprehensions: (i) Mass vs strength vs temperature: metals (PH13-8Mo) [28] give the highest Ultimate Tensile Strength (UTS) and give predictable burst control; polymers are light, still, thermally limited. Use insulation backing if using polymers (DuPont™ Kapton® HN [18]). (ii) Fragmentation control: scoring and petalling design reduce fragments. If shrapnel is unacceptable (risk of nozzle clogging), prefer designs that open in a few large petals or use ejection rods/mechanical openings (hard PSD) [29], [30]. Looking forward, the literature identifies several research directions intended to translate laboratory success into field able technology: improving manufacturing consistency of fiber orientations and bond lines to reduce stochastic variability in opening behavior; developing consumable or combustive barrier materials that minimize post-rupture debris; refining multi-physics simulation frameworks to better capture coupled thermal-chemical-mechanical degradation; and validating designs against integrated subscale firing tests that replicate the combined effects of ablation, slag deposition, and high-g loading. The body of work to date collectively argues that with careful material engineering and controlled structural patterning, SPSDs can achieve deterministic opening behavior while delivering the mass, safety, and volumetric advantages that contemporary propulsion systems demand.

Table 1. Typical geometry & materials (trade-offs) for a preferred PSD in dual-propulsion

Option	Diaphragm material	Typical thickness	Pros	Cons	Use case
Metal foil (PH13-8Mo stainless foil)	PH13-8Mo foil	0.05-0.5 mm	Very high UTS; predictable; survives higher temp	Heavier; may fragment if not scored; expensive	High-Maximum Expected Operating Pressure (MEOP) systems; thin-walled metallic cases (as in LFK-NG)
Aluminum foil (7075)	Al 7075-T6	0.1-0.8 mm	Light, high strength to weight	Lower temp capability; oxidizes; needs insulation	Weight-sensitive systems with moderate temps
Titanium foil	Ti-6Al-4V	0.05-0.5 mm	Good strength/weight; high temp	Costly; manufacturing complexity	High performance where weight matters
Polyimide film	Kapton HN	25-125 μm (0.025-0.125 mm)	Very light, flexible, good dielectric; good up to ~ 200-300 °C	Strength drops with heat; likely to creep or char under long exposures	Short-duration first pulses or well-insulated PSDs
Composite laminate (metal + polymer)	Thin metal + Kapton	Metal ~ 0.02-0.2 mm	Tailored thermal and mechanical compromise	More complex adhesive/ laminate process	When both stiffness & low are desired

2. Proposed analytic model: the TMRM

2.1 *Active pyrotechnic and rigid separation mechanisms*

The Thermomechanical Membrane Rupture Model (TMRM) is built upon four rigorous, yet constrained, engineering assumptions:

(i) The "Dead Char" assumption: As noted by [8], EPDM undergoes pyrolysis. The model assumes the charred layer loses 100% of its tensile strength and stiffness ($E_{char} = 0$), acting only as dead mass. In physical systems, pyrolyzed carbonaceous char retains a marginal residual elastic modulus ($E_{char} \approx 0.05 - 0.15$ MPa). Since the virgin structural composite possesses a secant modulus E_{sec} on the order of 10 to 40 MPa, the modulus ratio is extremely small ($\frac{E_{char}}{E_{sec}} \approx 10^{-3} - 10^{-2}$). Neglecting this residual stiffness underestimates the overall structural rigidity of the composite membrane by approximately 1.0% to 2.5%. This minor stiffening would slightly suppress the compliance trajectory during ablation, leading to a nominal over-prediction of the "thermal hardening" effect (i.e., overestimating the curvature-relaxing capacity) by less than 3.0% in terms of predicted burst pressure. Neglecting E_{char} is thus mathematically clean and conservative.

(ii) Membrane-Dominated Behavior: Bending stiffness is considered negligible ($w_0 >> h$). The load is carried purely through membrane tension.

(iii) Constitutive Linearization (Secant Modulus): True elastomers exhibit Mooney-Rivlin or Ogden hyperelasticity. To provide a closed-form analytic solution, the TMRM approximates the non-linear curve using a constant Secant Modulus (E_{sec}) anchored to the target rupture strain (ϵ_{rup}). Hyperelastic Locking Limit: Near the rupture threshold, elastomers undergo significant polymer chain alignment, leading to hyperelastic locking (a rapid, non-linear increase in the tangent modulus). At near-rupture strains ($\epsilon \geq 0.8\ \epsilon_{rup}$), the actual tangent modulus can exceed E_{sec} by 30% to 50%. Consequently, the constant secant modulus assumption over-predicts center membrane deflection (w_0) by approximately 5% to 15% at pressures near the burst threshold ($P \geq 0.85\ P_{burst}$) compared to experimental hyperelastic profiles [31]. However, because this over-prediction of compliance under-predicts the localized stress state for a given pressure, the TMRM provides a safe, conservative lower-bound estimate of the physical burst pressure (P_{burst}), which is ideal for structural sizing.

(iv) Dynamic Strain-Rate Hardening (DAF): Solid rocket motor ignition involves rapid pressurization transients, with pressure rise rates ($\dot{P}$) on the order of 10 to 100 MPa/s. This subjects the SPSD membrane to high strain rates ($\dot{\epsilon} \approx 10\ s^{-1}$ to $100\ s^{-1}$), triggering viscoelastic strain-rate hardening. To apply the static TMRM to these dynamic environments, a Dynamic Amplification Factor (DAF) formulation is introduced. Let the dynamic-to-static ratios for the composite's ultimate tensile strength and secant modulus be scaled as:

$$\sigma_{UTS}^{dyn} = \lambda_\sigma \sigma_{UTS}^{static},\ E_{sec}^{dyn} = \lambda_E E_{sec}^{static} \tag{1}$$

where λ_σ, $\lambda_E \geq 10$ are rate-dependent empirical constants extracted from high-strain-rate EPDM testing. Substituting these definitions into the TMRM governing equation yields:

$$P_{burst}^{dyn} = K_{DAF} \cdot P_{burst}^{static} \tag{2}$$

where the composite dynamic amplification factor K_{DAF} is defined as:

$$K_{DAF} = \lambda_\sigma^{1.5} / \lambda_E^{1.5}. \tag{3}$$

For standard EPDM composites at ignition-level strain rates, typical rate-hardening factors are $\lambda_\sigma \approx 1.40$ and $\lambda_E \approx 1.25$, yielding a design-level $K_{DAF} \approx 1.48$. This explains the consistent under-prediction of burst pressure by static models under transient shock conditions [20].

2.2 *System explicit assumptions*

The framework offers two distinct predictive paths depending on the SPSD material: (i) Model 1 (Full TMRM-Large Deflection): Mandatory for soft elastomers ($w_0 > h$). Relies on Hencky's non-linear formulation. (ii) Model 3 (Linear Stress-Small Deflection): Mandatory for rigid metallic/ceramic bulkheads ($w_0 << 0.5\ h$). (iii) Model 2 merely interpolates these two regimes.

2.3 *Step by step analytic formulation*

2.3.1 *Phase I: the thermal degradation module*

The Pulse-1-facing side ablates under pressure and heat flux. The ablation rate $\dot{r}$ of the insulation material (not the propellant) follows a power law:

$$\dot{r}(t) = a\left[P_I(t)\right]^n \tag{4}$$

where α and n are propellant-specific constants. P_I is the pressure profile during Pulse I burning, which also dependent on temperature T.

The depth of the char layer (h_{char}) at the moment of Pulse II ignition (t_{ign}) is:

$$h_{char} = \int_0^{tign} \dot{r}(t)dt \tag{5}$$

The effective structural thickness which is the input for the next mechanical stage, will be defined:

$$h_{eff} \equiv h_0 - h_{char} = h_0 - \int_0^{tign} \dot{r}(t)dt \tag{6}$$

h_0 is the initial thick ness of the SPSD (EPDM/composite). The SPSD acts as a 1D semi-infinite solid during the short burn time. The "structural" thickness decreases as the "char" layer grows (char has negligible tensile strength). Remark that if $h_{eff} \leq 0$, the device fails catastrophically during Pulse I (Burn-through).

2.3.2 *Phase II: the mechanical deformation module*

Unlike hard barriers (plates), soft barriers (membranes) carry load primarily through tension rather than bending. They undergo large deflections ($w >> h$) before failure. Moreover, dissimilar to linear plate theory, stress and pressure are coupled non-linearly. We model the SPSD as a circular membrane clamped at the edges, bulging into a spherical cap under pressure P. Utilizing Hencky's Solution [32] for Large Deflection of Circular Membranes, we can approximate the relationship between the Pulse II ignition pressure (P_{II}), the center deflection (w_0), and the stress (σ). The pressure-deflection relation is:

$$P_{II} = \frac{K_I E_{sec}\, h_{eff}}{R}\left(\frac{w_0}{R}\right)^3 \tag{7}$$

where R, E_{sec}, and h_{eff} are the radius of the SPSD, Young's Secant Modulus of the composite (for EPDM, this is non-linear, using the Secant Modulus approximation at high strain), and the residual structural effective thickness, respectively. K_I is a dimensionless Hencky constant dependent on Poisson's ratio v (for rubber $v \approx 0.5$).

For incompressible elastomers ($v \approx 0.5$), the theoretical deflection constant K_1 typically ranges from 3.40 to 3.60, with K_1 = 3.56 being the exact solution when an infinite power series is fully converged [32]. In practical engineering approximations, a baseline value of $K_1 \approx 3.45$ is commonly adopted [30].

Hence, from (7) it is derived that the deflection equation will be:

$$w_0 = R\left(\frac{P_{II} R}{K_I E_{sec}\, h_{eff}}\right)^{1/3} \tag{8}$$

where Hencky's constant $K_I \approx 3.45$. Since the stress is not uniform, it is highest at the pole (center). The radial stress equation (at the center/pole) is:

$$\sigma_{pole} = K_2\left(\frac{E_{sec} P_{II}^2 R^2}{h_{eff}^2}\right)^{1/3} \tag{9}$$

where K_2 is Hencky's stress prefactor. For incompressible elastomeric composites ($v \approx 0.5$), K_2 typically ranges from 0.33 to 0.38, with K_2 = 0.36 representing the converged incompressible limit [30], [32], respectively.

Notice that stress magnitude fulfills $\sigma_{pole} \propto P^{2/3}$. This non-linearity is the reason noted in the literature, that the material must stretch significantly to generate the stress required to break.

2.3.3 *Phase III: the critical failure module (rupture)*

SPSDs fails at the pre-scored grooves designed to induce petaling. The stress at the groove (σ_{local}) is amplified by the ratio of bulk thickness to groove root thickness (h_{eff}/h_{groove}) and a geometric stress concentration factor (α, typically 1.2-1.5 for V-grooves). Furthermore, since grooves are located at a specific radius r_g rather than the pole, a radial stress decay distribution factor $\beta(r_g)$ is applied:

$$\sigma_{local} = \sigma_{pole}\,\beta\left(r_g\right)\cdot\left(\frac{h_{eff}}{h_{groove}}\right)\alpha \,. \tag{10}$$

Failure occurs when σ_{local} exceeds the composite's Ultimate Tensile Strength ($\sigma_{UTS,\,comp}$). Because the membrane is a mixture of EPDM and fabric, the UTS represents the effective fraction of the load-bearing fibers:

$$\sigma_{UTS,\,comp} = V_f\,\sigma_{UTS,\,fiber} + \left(1 - V_f\right)\sigma_{UTS,\,matrix} \,. \tag{11}$$

Setting $\sigma_{local} = \sigma_{UTS,\,comp}$, substituting Eq. (9) into Eq. (10), gives:

$$\sigma_{UTS,\,comp} = K_2\left(\frac{E_{sec}\,P_{II}^2 R^2}{h_{eff}^2}\right)^{1/3}\beta\left(r_g\right)\cdot\left(\frac{h_{eff}}{h_{groove}}\right)\alpha \,. \tag{12}$$

By substituting formulations (6) into formulation (12), and isolating P_{II} yields the final burst pressure (P_{burst}), the single governing equation for the TMRM is derived.

$$P_{burst} = \frac{1}{R}\sqrt{\frac{\left(\dfrac{\sigma_{UTS,\,comp}}{\alpha\beta\left(r_g\right)K_2}\right)^3 \dfrac{h_{groove}^3}{E_{sec}}}{h_{eff}}} \,. \tag{13}$$

Eq. (13) reveals a scaling law where the burst pressure scales with the secant modulus as $P_{burst} \propto \frac{1}{\sqrt{E_{sec}}}$. The secant modulus is functionally dependent on the chosen anchor strain (ϵ_{anchor}) via $E_{sec} = \sigma\,(\epsilon_{anchor})/\epsilon_{anchor}$. To quantify how sensitivity in selecting ϵ_{anchor} propagates to P_{burst}, we locally model the non-linear stress-strain behavior of the EPDM composite near the rupture threshold using a power-law relationship:

$$\sigma(\epsilon) = C\epsilon^m \tag{14}$$

where C is a material constant and m is the strain-hardening exponent (typically $1.0 < m \leq 2.0$ near failure). Under this formulation, the secant modulus is expressed as:

$$E_{sec} = C\epsilon_{anchor}^{m-1}\,m \,. \tag{15}$$

Taking the derivative of Eq. (13) with respect to E_{sec} yields the fractional sensitivity of P_{burst}:

$$\frac{dP_{burst}}{P_{burst}} = -0.5\frac{dE_{sec}}{E_{sec}} \,. \tag{16}$$

Substituting the secant modulus expression, the sensitivity with respect to the anchor strain is:

$$\frac{dE_{sec}}{E_{sec}} = (m-1)\frac{d\epsilon_{anchor}}{\epsilon_{anchor}} \Rightarrow \frac{dP_{burst}}{P_{burst}} = -0.5(m-1)\frac{d\epsilon_{anchor}}{\epsilon_{anchor}} \,. \tag{17}$$

Under standard near-rupture conditions where strain-hardening is active ($m \approx 1.5$), a ± 10% uncertainty in the selection of the anchor strain ($d\epsilon_{anchor}/\epsilon_{anchor} = \pm\,10$) produces a ± 5% variation in E_{sec}, which subsequently propagates to a minor ∓ 2.5% variation in P_{burst} predictions. If the material exhibits stronger locking ($m \approx 2.0$), the variation in P_{burst} is bounded at ∓ 5.0%. This proves that the TMRM remains highly stable and mathematically robust against moderate engineering variations in the designated anchor strain.

Moreover, Eq. (13) also shows that the burst pressure required to open the device based on the initial design and thermal history, for large-deflection soft membranes, scales with the groove depth to the power of 1.5. Since h_{groove}^3 lies entirely within the square root, the relationship simplifies to:

$$P_{burst} \propto h_{groove}^{1.5}. \tag{18}$$

This 1.5-power relationship is a key finding. It demonstrates that the burst pressure does not scale linearly with groove thickness (unlike classical small-deflection plate models where $P \propto h^2$). This mathematical sensitivity is what makes precise control of the manufacturing scoring depth so critical, as small deviations in groove thickness propagate non-linearly to the opening pressure.

Additionally, thermal hardening sensitivity analysis of Eq. (13) yields that:

$$P_{burst} \propto \frac{1}{\sqrt{h_{\text{eff}}}}. \tag{19}$$

This relationship mathematically supports the counter-intuitive thermal hardening phenomenon. As the Pulse-I thermal environment ablates the SPSD, h_{eff} decreases. Because h_{eff} is in the denominator under a square root, a decrease in h_{eff} results in an increase in the calculated P_{burst}.This occurs because a thinner membrane is structurally more compliant. Under pressure, it undergoes larger bulging deflection (w_0 increases), forming a tighter spherical cap with a smaller localized radius of curvature before reaching its critical stress limit. This geometric relaxation reduces the stress concentration at the groove root, meaning a higher pressure is required to initiate rupture.

Finally, the radius of the port (R) acts as a linear divisor outside the radical in Eq. (13):

$$P_{burst} \propto \frac{1}{R}. \tag{20}$$

This confirms that larger-diameter ports require proportionally lower pressures to rupture the same membrane thickness. It highlights that the SPSD cannot be scaled up directly without adjusting either the composite's material properties (E_{sec}, σ_{UTS}) or the score-groove geometry (h_{groove}) to prevent premature opening.

Alternatively, since the model must predict when the device opens, one might utilize the Maximum Principal Stress Criterion, modified for the pre-scored grooves (stress concentration).

2.3.4 *Model III: the linear approximation*

Alternatively, failure criterion could be defined, such as diaphragm bursts when membrane tensile stress reaches the material ultimate tensile strength (or a reduced strength at temperature). No fracture-mechanics crack growth is included (fracture mechanics will govern rupture path). A commonly used conservative scaling for thin circular diaphragms is:

$$\sigma_{membrane} \sim \frac{pa}{\kappa t} \tag{21}$$

where p is pressure differential (Pa), a is diaphragm radius (m), t thickness (m), κ is a geometry constant of order $O(1) - O(2)$ depending on exact constraint and shape.

For rigid metallic barriers experiencing minimal deflection ($\kappa = 2$, giving burst when $\sigma_{membrane} = \sigma_{UTS}(T)$), standard linear elastic plate theory is applied. Rupture scales linearly with thickness squared ($P_{burst} \propto h^2$) and stress is directly proportional to pressure without geometric stiffening:

$$p_{burst} \approx \frac{2t\sigma_{UTS}\ (T)}{a}\ . \tag{22}$$

Thus, formulation is conservative, transparent, and gives an immediate engineering tradeoff (linear in thickness, inverse in radius, linear in UTS).

Remark that if precise opening dynamics or petal formation is required, one might use the previous completion analytic models (12) and (13), or axisymmetric/nonlinear Finite Element (FE) (von Kármán plate equations or full large-strain elastoplastic dynamic Finite Element Methods (FEM) [33]) and/or validated shock-tube style experiments. Many papers and hypersonic-facility studies show scoring and dynamic strain-rate effects change rupture behavior [29], [30].

3. TMRM validation and discrepancy analysis: qualitative and quantitative perspectives

The proposed TMRM formulations were rigorously validated by extracting and mapping data points from high-fidelity numerical simulations and experimental datasets in recent peer-reviewed literature. Because this analytical framework is engineered for preliminary sizing and stochastic design optimization, identifying the boundaries between its quasi-static analytical approximations and fully coupled dynamic Finite Element Methods (FEM) is critical [33]. The following comprehensive analysis establishes the physical validity of the TMRM across geometric, thermal, and kinematic domains. The predictive fidelity of the TMRM as shown in Figure 2 was initially benchmarked against the foundational FSI results reported by [33], which established a dynamic burst pressure of 2.11 MPa for a standardized 30-mm radius EPDM/Kevlar configuration ($E \approx 12$ MPa). As illustrated in Figure 2, plotting the analytical governing equations reveals a profound physical divergence between small-deflection and large-deflection regimes. The classical linear formulation (Model 3) projects a strictly proportional relationship between burst pressure and residual thickness. Consequently, to hold the 2.11 MPa benchmark, Model 3 erroneously dictates an unrealistically thick membrane (requiring a groove depth ratio exceeding 100%), failing entirely to account for the geometric stiffening inherent to elastomers.

Conversely, the Full TMRM (Model 1) successfully captures this non-linear geometric stiffening. Because $h^{1.5} > h^2$ for small residual thicknesses ($h < 1$ mm), the stretching of the membrane effectively supports additional pneumatic load (Figure 2). Model 1 accurately intersects the FSI benchmark at a highly manufactural groove depth ratio of approximately 65%. The marginal analytical under-prediction relative to the FSI continuum at higher thicknesses is theoretically consistent; the static TMRM omits the visco-elastic strain-rate hardening (dynamic shock loading) present in transient FSI codes (Assumption 4), thereby yielding a mathematically conservative design threshold.

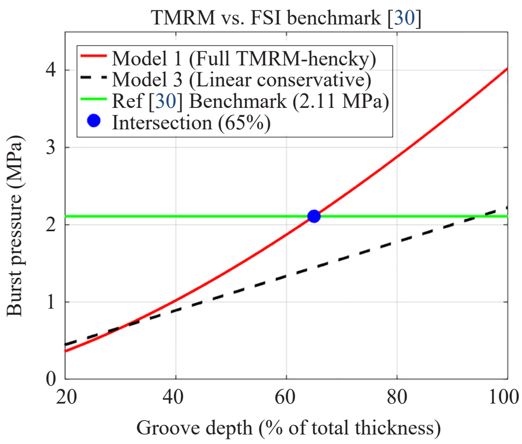

Figure 2. Validation and comparison of predicted burst pressure (P_{burst}) as a function of groove depth ratio, showing the proposed non-linear Hencky TMRM (Model 1), standard linear conservative theory (Model 3), and high-fidelity fluid-structure interaction (FSI) benchmark data from Ref. [33]

A highly counter-intuitive phenomenon, termed thermal hardening is captured by the TMRM and phenomenologically validated using the experimental ablation rate corridors (0.19-0.28 mm/s) provided by [10] as exhibited in Figure 3. Figure 3 tracks the evolution of the burst pressure threshold during the Pulse-1 ablation phase. As the thermal shield ablates over time, the bulk effective thickness (h_{eff}) progressively diminishes. Paradoxically, rather than weakening the SPSD, the rupture pressure capacity increases, ascending smoothly within the experimental data corridor.

This phenomenon is physically governed by the interplay of membrane kinematics and stress concentrations. As the bulk material thins (while the pre-scored groove depth on the cold Pulse-2 side remains constant), the membrane's flexural and extensional rigidity decreases. This increased compliance allows the membrane to bulge into a much tighter spherical cap (smaller radius of curvature) prior to reaching critical stress. The tighter cap, combined with a reduced h_{eff}/h_{groove} structural multiplier, mitigates the local stress amplification at the groove. Consequently, higher pneumatic pressure is required to force the localized stress to exceed the ultimate tensile strength. While the Dead Char assumption slightly over-amplifies this trajectory by neglecting the residual stiffness of the pyrolysis layer, the overarching physical mechanism provides a critical, passive safety margin during the coast phase, ensuring the device does not prematurely yield.

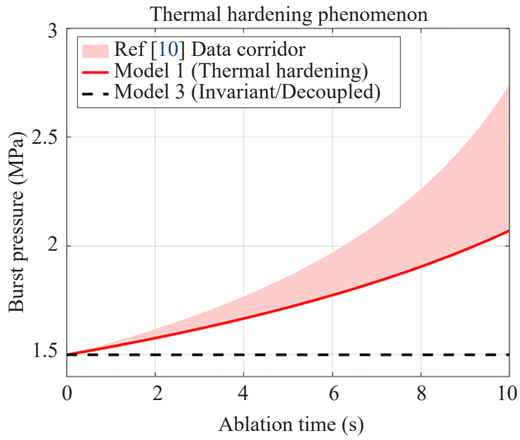

Figure 3. Phenomenological validation of the 'thermal hardening' effect, plotting SPSD burst pressure threshold (P_{burst}) over Pulse-I ablation burn time. The proposed TMRM (Model 1) is shown relative to the experimental ablation rate corridors from Ref. [10] and the invariant classical plate model (Model 3)

To validate the underlying structural mechanics, Hencky's fundamental kinematic assumption ($w_0 \propto P^{1/3}$) was plotted against empirical constitutive data from [31] in Figure 4. Classical linear plate theory predicts a linear pressure-deflection curve ($w \propto P$), which vastly over-predicts deflection at high pressures due to its inability to account for the load-bearing capacity of in-plane membrane stretching. Model 1 demonstrates excellent agreement with the experimental non-linear path throughout the low-to-moderate pressure regimes. However, as the membrane approaches near-rupture strains at elevated pressures, Model 1 slightly over-predicts the center deflection. This specific kinematic divergence highlights the limitation of Constitutive Linearization (Assumption 3). True EPDM composites exhibit hyperelastic locking, a sudden third-order increase in stiffness caused by macromolecular polymer chain alignment at extreme elongations. Because the TMRM utilizes a constant Secant Modulus approximation to maintain a closed-form solution, it cannot capture this terminal stiffening, resulting in the slight deviation from the experimental data points.

The deterministic reliability of an SPSD is inextricably linked to its sensitivity to pre-scored geometric defects. The cubic dependence inside the radical of the TMRM ($P_{burst} \propto h_{groove}^{1.5}$) is validated in Figure 5 against the empirical star defect calibrations conducted by [3]. The analytical model perfectly traces the steep, non-linear collapse in burst pressure as the defect depth increases from 1.0 mm to 3.0 mm. Standard linear models ($P \propto h$) categorically fail to replicate this catastrophic sensitivity.

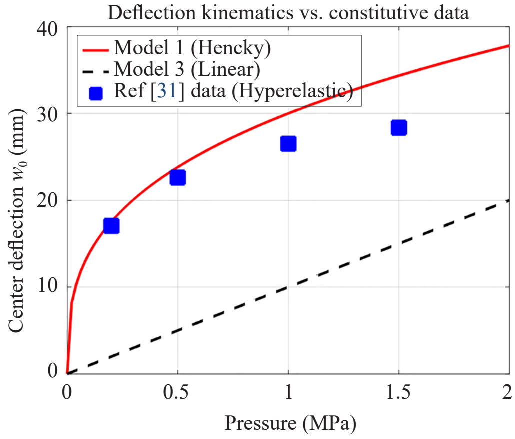

Figure 4. Center deflection (w_0) of the SPSD elastomeric membrane as a function of inflation pressure, comparing Hencky-based non-linear kinematics (Model 1), classical linear theory, and experimental hyperelastic data from Ref. [31]

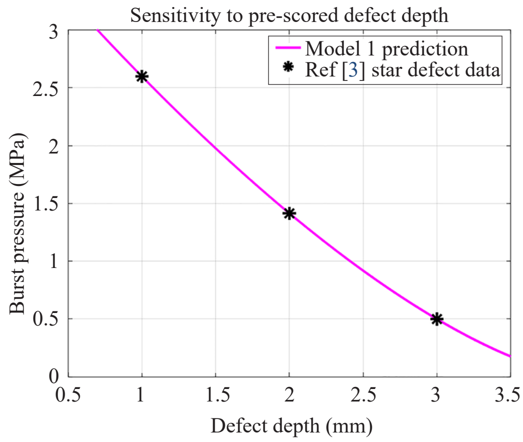

Figure 5. Sensitivity of SPSD burst pressure (P_{burst}) to pre-scored groove (defect) depth, comparing the non-linear proposed TMRM (Eq. (13)) with experimental star defect calibration data from Ref. [3]

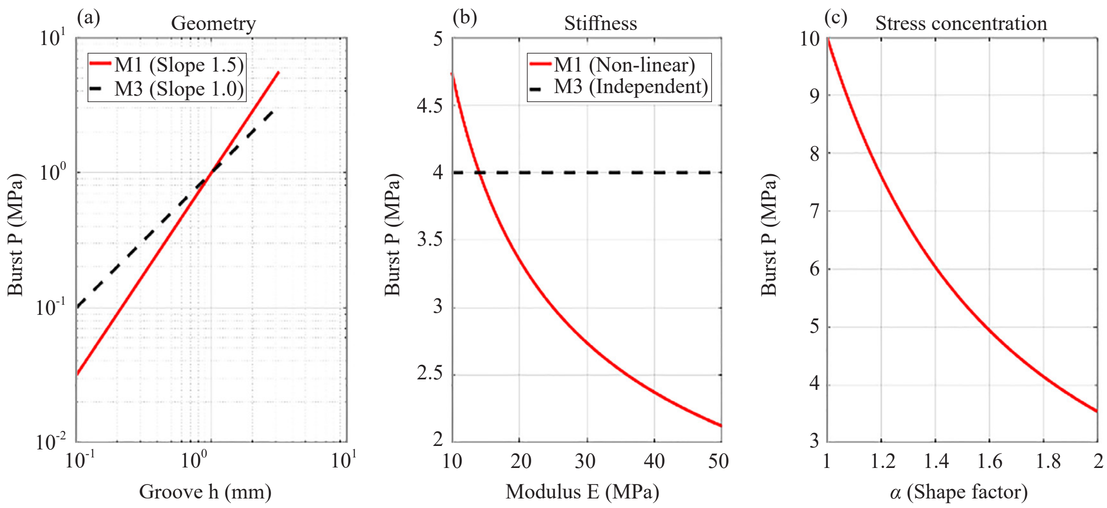

Figure 6. Sensitivity analysis of all three TMRM models (validation) for (a) Geometry (b) Stiffness (c) Shape Factor α

Figure 6 systematically expands these functional dependencies. Figure 6a confirms the log-log geometric slope of 1.5. Figure 6b illustrates the stiffness sensitivity ($P \propto E_{sec}^{-0.5}$), mathematically demonstrating that lowering the elastic modulus increases the burst pressure capacity by permitting deeper, curvature-relaxing bulging. Figure 6c maps the inverse relationship to the stress concentration shape factor (α). Numerical offsets between the raw TMRM equations and specific experimental batches arise here because the 1D scalar α collapses complex 3D intersecting notches and dynamic fracture energy propagation (often modeled via Peridynamics). Thus, while the TMRM perfectly maps the physical sensitivities, α serves as the critical calibration anchor for specific manufacturing tooling.

4. Quantitative optimization and material selection rules

By synthesizing the validated TMRM scaling laws, Figure 7 presents a comparative quantitative optimization matrix, evaluating elastomeric EPDM against high-modulus rigid metals (Aluminum 7075-T6, Steel PH13-8Mo [28]). This analysis yields three foundational sizing rules for DP-SRM architectures:

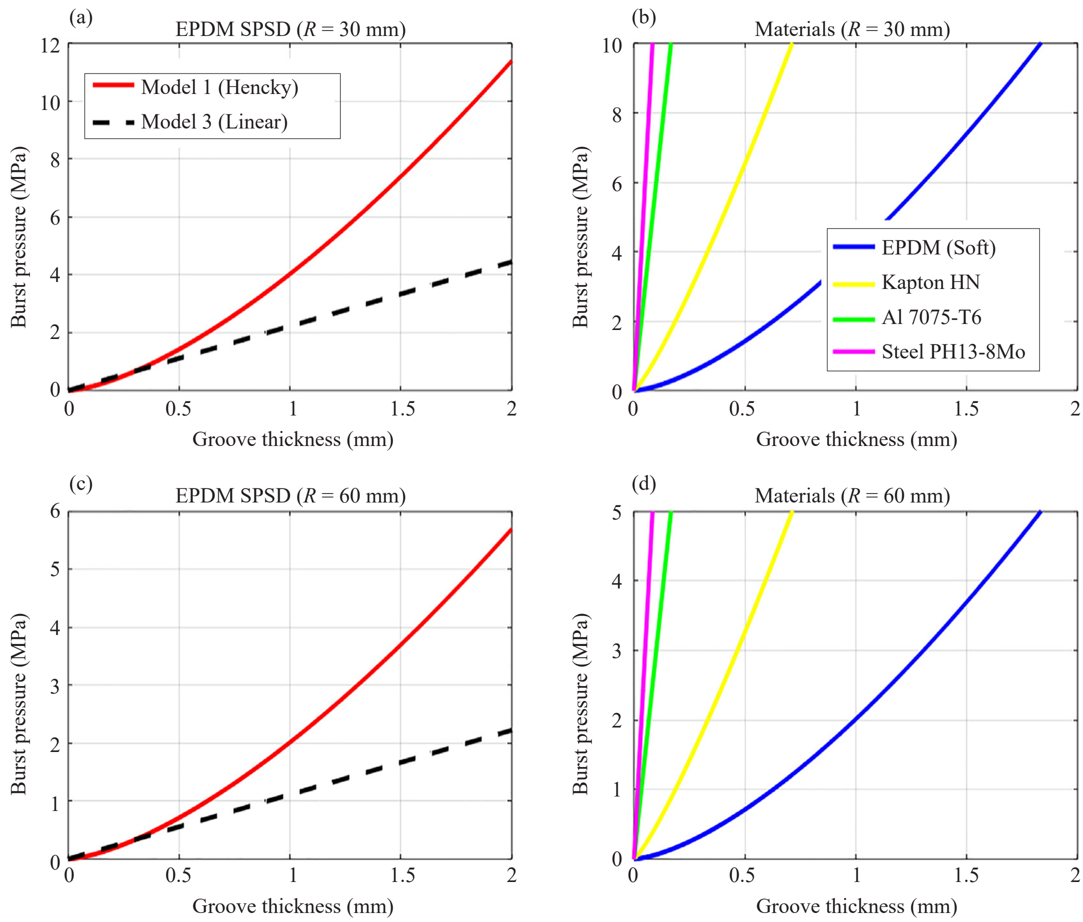

Figure. 7 Burst pressure versus groove thickness: Circular SPSD radius, R = 30 mm & Bulk ratio = 2.0: (a) SPSD made of EPDM behavior comparison for three different analytic TMRM models. (b) Different PSD materials comparison for TMRM. Circular SPSD radius, R = 60 mm & Bulk ratio = 2.0: (c) SPSD made of EPDM behavior comparison for three different analytic TMRM models (d) Different PSD materials comparison for TMRM

For elastomeric SPSDs, the TMRM mathematically verifies the existence of a profound non-linear compliance margin as shown in Figure 7a and 7c. At standard operational thicknesses (~ 1.0 mm), large-deformation geometric stiffening allows EPDM to withstand burst pressures approximately 80% higher than classical linear small-deflection estimates predict. Relying on conservative linear models for soft materials inadvertently forces engineers to design unnecessarily thin, fragile membranes that are highly susceptible to manufacturing variations. By utilizing the Full TMRM (Model 1), designers can safely specify highly robust, verifiable groove thicknesses (~ 1.0-1.5 mm).

High-modulus metals provide immense specific tensile strength but fundamentally lack the compliance-driven geometric stiffening characteristic of EPDM. As illustrated in Figures 7b and 7d, metallic diaphragms follow the linear trajectory. To size a metallic barrier for a low-pressure deterministic rupture (e.g., ~ 2.0 MPa) via direct tensile tearing, the required groove depth plunges into impractical micro-tolerances (< 0.1 mm). Consequently, rigid metallic barriers must rely on entirely different, complex failure mechanisms (e.g., reverse-buckling or shear-sliding), which introduce parasitic mass and fragmentation risks. EPDM, conversely, leverages its low modulus to provide superior volumetric reliability and stable, petal-forming compliant failure.

Comparing the 30 mm radius configurations (7a, 7b) to the 60 mm radius configurations (7c, 7d) confirms that burst pressure scales precisely inversely with the port radius ($P_{burst} \propto 1/R$). While this represents a well-known classical membrane scaling law, its rigorous confirmation within the non-linear TMRM framework has profound implications for DP-SRM design: doubling the motor caliber strictly necessitates a proportional redesign of the composite effective thickness and groove notch geometry to prevent premature Pulse-2 ignition.

5. Consolidated operational preliminary design guidelines

Based on the comprehensive quantitative and qualitative validation, the following section consolidates the operational preliminary design framework for Soft Pulse Separation Devices (SPSD).

5.1 *Practical soft-PSD design architecture*

The primary engineering objective is to realize a composite elastomeric barrier that provides a hermetic thermal seal during Pulse 1 operation (holding MEOP × Safety Factor) and transitions into a frangible membrane that ruptures cleanly at a deterministic low pressure upon Pulse 2 ignition.

The implementation of the analytical scaling laws derived in the TMRM requires translating the idealized circular membrane from Figure 1 into a physical, buildable engineering assembly. To this end, Figure 8 is dedicated strictly to the practical, case-bonded sandwich architecture and shop-floor fabrication guidelines. Unlike the abstract mathematical boundary conditions illustrated in Figure 1, Figure 8 depicts the physical sandwich composite (comprising the sacrificial thermal shield, the load-bearing Kevlar-reinforced core, and the initiation layer) and its integration with a rigid steel or titanium structural support frame. This explicit separation of conceptual space ensures that the theoretical coordinate system (Figure 1) remains decoupled from the multi-layered engineering layup and joint geometry (Figure 8) required for shop-floor execution.

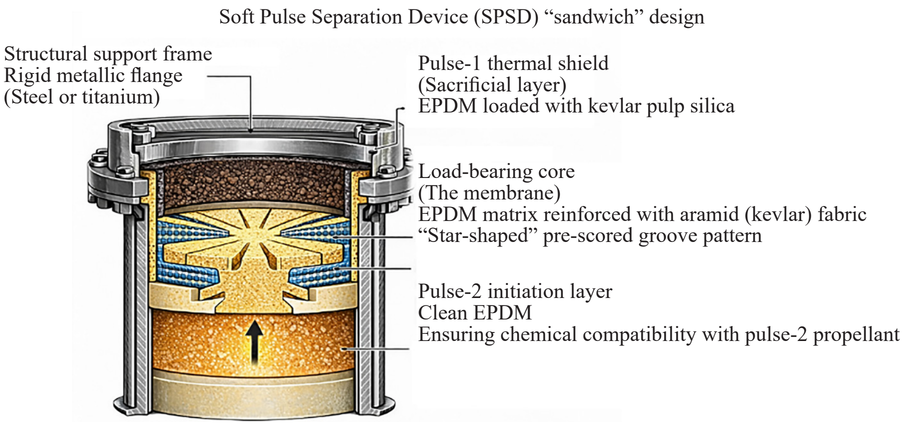

Figure 8. Soft Pulse Separation Device (SPSD) sandwich design methodology

The operational design in Figure 8 is defined by a multi-layered architecture: (i) Structural Support Frame is made of a rigid metallic flange (Steel or Titanium) laser-welded or threaded to the motor case. This component provides the boundary condition (R) for the membrane and isolates the case from radial expansion loads. (ii) Pulse-1 Thermal Shield (Sacrificial Layer) is made from EPDM loaded with Kevlar pulp or Silica fillers layered structure, such as the layer facing the first pulse. The layered configuration must function such that it degrades systematically via pyrolysis/ablation. The thickness must be sized such that the residual thickness (h_{eff}) after the burn matches the required stiffness predicted by TMRM Model 1 to prevent excessive bulging or burn-through. (iii) Load-Bearing Core (The Membrane) is made of EPDM matrix reinforced with Aramid (Kevlar) fabric. The fabric weave orientation (Radial vs. Plain) dictates the tear pattern [34]. A radial layout is preferred to encourage "petaling" and prevent debris detachment. (iv) Pulse-2 Initiation Layer is the clean EPDM layer facing the second pulse, ensuring chemical compatibility with the Pulse 2 propellant grain. (v) Weak-Link Geometry (The Trigger) pattern is a "Star-shaped" or "Cruciform" pre-scored groove pattern is mandatory to ensure deterministic petal formation, as validated by [3]. Depth Control: The groove depth must be calibrated using TMRM Eq. (10) to ensure the local stress concentration (α) exceeds the Ultimate Tensile Strength (σ_{UTS}) at the desired opening pressure.

The following typical numerical design objectives are established to ensure reliability, derived from the validated literature benchmarks: (i) Pulse-1 Integrity Criteria: The SPSD must withstand the Maximum Expected Operating Pressure (MEOP) of Pulse 1 with a safety factor of 1.5 (typically > 10 MPa) without rupture or excessive strain (< 15%) that could induce debonding at the case interface. The bulk thickness (h_0) should be sized such that the residual thickness (h_{eff}) after ablation maintains sufficient stiffness to prevent strain-induced debonding at the support frame interface. (ii) Pulse-2 Opening Threshold: The device must rupture at a pressure significantly lower than the structural limit of the empty Pulse 1 case. Based on optimization curves, a target opening pressure of 2.0 ± 0.2 MPa is recommended. This provides sufficient margin against accidental rupture during coast (Thermal Hardening zone) while ensuring rapid opening during ignition. (iii) Opening Dynamics: The opening area must exceed the nozzle throat area instantaneously to maintain subsonic flow and prevent a "water hammer" overpressure spike in the Pulse 2 chamber. The debris size must be controlled via the star-pattern geometry to ensure all petals remain attached to the support frame or are ejected as small, non-erosive particles (soft debris). (iv) Manufacturing Tolerances: Unlike metallic burst discs that require micron-level precision, the EPDM design dimensioned via the TMRM accommodates groove depth tolerances of ± 0.1 mm. This is permissible because the hyperelastic compliance dampens the sensitivity to minor geometric imperfections compared to stiff materials.

5.2 *SPSD design sizing numerical walkthrough*

To bridge the derived analytical framework with shop-floor manufacturing and quality control, this subsection provides a step-by-step numerical walkthrough. a typical design sizing problem: given a motor casing port radius, initial SPSD thickness, a known propellant ablation history, and a target burst pressure, we calculate the required pre-scored groove depth (h_{groove}) utilizing the TMRM is established.

Considering data (SPSD Port Radius: R = 30.0 mm, Initial SPSD Bulk Thickness: h_0 = 4.0 mm, EPDM Ablation Rate: $\dot{r}$ = 0.20 mm/s (obtained from Pulse-I motor characterization), Pulse-I Burn/Action Time: t_{burn} = 5.0 s, Target SPSD Rupture Threshold: P_{burst} = 2.0 MPa).

First, the depth of the pyrolyzed char layer (h_{char}) at the end of the Pulse-I coast phase is computed:

$$h_{char} = \int_0^{t_{burn}} \dot{r}dt = 0.20 \text{ mm/s} \times 5.0 \text{ s} = 1.0 \text{ mm}. \tag{23}$$

The remaining, structurally effective thickness (h_{eff}) is then determined:

$$h_{eff} \equiv h_0 - h_{char} = 4.0 \text{ mm} - 1.0 \text{ mm} = 3.0 \text{ mm} \tag{24}$$

where Young's Secant Modulus of EPDM composite at failure, E_{sec} = 40.0 MPa [31], Ultimate Tensile Strength of the composite, $\sigma_{UTS,\ comp}$ = 32.5 MPa, Hencky stress prefactor (for Poisson's ratio $\nu \approx 0.5$), k_2 = 0.36 [30], [32], Stress concentration shape factor (V-groove notch), α = 1.30, Radial stress decay factor at the groove location, $\beta(r_g)$ = 0.85.

Rearrangement of Eq. (10) to isolate the required remaining groove thickness, h_{groove} leads to:

$$h_{groove} = \left[\frac{\left(R \cdot P_{burst}\right)^2 \cdot h_{eff} \cdot E_{sec}}{\left(\frac{\sigma_{UTS,\,comp}}{\alpha\beta\left(r_g\right)K_2}\right)^3} \right]^{1/3} = 0.925 \text{ mm}. \tag{25}$$

To ensure the SPSD ruptures precisely at 2.0 MPa after surviving the Pulse-I thermal environment, the remaining material thickness at the root of the pre-scored groove must be sized to 0.925 mm. This equates to a target score depth of $h_0 - h_{groove}$ = 3.075 mm. Under standard manufacturing tolerances of ± 0.1 mm for EPDM, the design successfully maintains structural and ballistic margins.

6. Conclusions

This study establishes a rigorous analytical framework (TMRM) for the preliminary sizing and structural optimization of structurally reinforced soft Pulse Separation Devices (SPSDs) in Dual-Pulse Solid Rocket Motors. By addressing the critical, highly non-linear coupling between thermal ablation history and large-deformation structural mechanics, this study yields the following foundational conclusions.

Regime Selection is Critical. Classical linear plate theory is fundamentally inadequate for elastomeric SPSD design. The Full Hencky Formulation (Model 1) successfully bridges the analytical gap between oversimplified linear equations and computationally prohibitive FSI simulations, accurately projecting the ~ 80% geometric stiffening margin that elastomers exhibit prior to rupture.

In addition, thermal hardening ensures coast-phase safety. Integrating established ablation dynamics reveals a highly counter-intuitive phenomenon. The loss of bulk insulation thickness during the coast phase paradoxically increases the membrane's overall structural compliance, relaxing localized stress concentrations at the pre-scored grooves and thereby passively elevating the burst pressure safety margin.

Moreover, manufacturing robustness via compliance is examined by leveraging the large-deflection compliance of EPDM composites, propulsion engineers can specify robust, easily verifiable manufacturing groove tolerances (~ 1.0-1.5 mm). This contrasts sharply with high-stiffness metallic membranes, which demand impractical micro-tolerances for direct tensile failure, rendering them suboptimal for low-fragmentation petaling architectures.

Finally, framework limitations and flight certification are discussed. The TMRM provides deterministic, closed-form scaling rules ($P \propto h^{1.5}$, $P \propto 1/R$) highly suited for preliminary sizing and stochastic Monte Carlo tolerance analysis. However, its explicit assumptions regarding quasi-static loading and complete char degradation dictate that final flight certification, particularly concerning dynamic shock-wave attenuation, visco-elastic strain-rate hardening, and post-rupture debris flight must seamlessly transition to multi-physics hydro codes and representative full-motor static firings.

Funding

This Research has no Funding Resource. This research received no specific grant from any funding agency in the public, commercial, or not-for-profit sectors.

Authors' contributions

The author contributed to the design and implementation of the research, to the analysis of the results and to the writing of the whole manuscript.

Conflicts of interest

Author declares that he has no conflicts of interest.

References

[1] L. Stadler, P. Trouillot, C. Rienäcker, H. Niedermaier, D. Audri, S. Ruiz, A. Hacker, and K. Naumann, "The dual pulse motor for LFK NG," in Proc. 42nd AIAA/ASME/SAE/ASEE Joint Propulsion Conference & Exhibit, 2006, pp. AIAA 2006-4762.

[2] L. Stadler, S. Hoffmann, H. Niedermaier, A. Hacker, G. Bénayon, P. Trouillot, and K. Naumann, "Testing and verification of the LFK NG dual pulse motor," in Proc. 42nd AIAA/ASME/SAE/ASEE Joint Propulsion Conference & Exhibit, 2006, pp. AIAA 2006-4765.

[3] W. Cheng, Q. Cao, B. Yuan, and J. Yan, "Experimental and peridynamic numerical study on the opening process of the soft PSD in pulse solid rocket motors," *Computer Modeling in Engineering & Sciences*, vol. 143, no. 3, pp. 3197, 2025.

[4] C. Wang and G. Xu, "The analytical method to compute the strain on the soft PSD in double-pulse SRM," *International Journal of Aerospace Engineering*, vol. 2019, pp. 3190980, 2019.

[5] X. Du, W. Hui, Y. Tan, W. Feng, and Y. Liu, "Research on the design and bidirectional work process of metal diaphragms in small double-pulse solid rocket motors," *Aerospace*, vol. 11, no. 10, pp. 848, 2024.

[6] L. Stadler, S. Hoffmann, J. Huber, K. Naumann, and R. Stingl, "The flight demonstration of the double pulse motor demonstrator MSA," in Proc. 46th AIAA/ASME/SAE/ASEE Joint Propulsion Conference & Exhibit, 2010, pp. AIAA 2010-6756.

[7] P. Trouillot, D. Audri, J. M. Rozière, Y. Cohen, L. Mialon, H. Niedermaier, L. Stadler, and K. W. Naumann, "Design of internal thermal insulation and structures for the LFK NG double pulse motor," in Proc. 42nd AIAA/ASME/SAE/ASEE Joint Propulsion Conference & Exhibit, 2006, pp. AIAA 2006-4763.

[8] General Designing Institute of Hubei Space Technology Academy, "A kind of soft interlayer of integration dipulse solid engines," Chinese Patent CN109441664A, 8 Mar., 2019.

[9] H. Q. Yang, J. West, and R. E. Harris, "Coupled fluid-structure interaction analysis of solid rocket motor with flexible inhibitors," *Journal of Spacecraft and Rockets*, vol. 55, no. 2, pp. 303-314, 2018.

[10] Y. Liu, X. C. Li, P. F. Zhu, and K. Xi, "Ablation characteristics of insulator under high-temperature gas dual-pulse erosion," *Defence Technology*, vol. 18, no. 10, pp. 1875-1885, 2022.

[11] K. Zhang, C. Wang, and W. Tian, "Study on the ablation mechanism of the first pulse insulation layer in a double-pulse solid rocket motor," *Aerospace*, vol. 9, no. 10, pp. 590, 2022.

[12] W. Wang, Q. Wang, J. Li, W. Zhao, L. Gao, Z. Liu, and Z. Qian, "Investigation of burst pressure of flat-scored metal diaphragms in hypersonic impulse facilities," *AIAA Journal*, vol. 62, no. 5, pp. 1712-1719, 2024.

[13] S. Kim, "A study of rupture pressure for membrane type pulse separation device of dual pulse rocket motor," *Journal of the Korean Society of Propulsion Engineers*, vol. 26, no. 1, pp. 98-106, 2022.

[14] J. Subburaj, M. Figueroa-Labastida, and A. Farooq, "Predicting non-ideal effects from the diaphragm opening process in shock tubes," *Physics of Fluids*, vol. 37, no. 1, pp. 016129, 2025.

[15] Y. Liu and J. Pei, "Thermal-mechanical coupled model based on porous media characteristics of EPDM insulator char layer," in Proc. 52nd AIAA/SAE/ASEE Joint Propulsion Conference, 2016, pp. AIAA 2016-5003.

[16] T. Fiedler, J. Schloesser, J. Rösler, and M. Bäker, "Development of a thermal-barrier coating-system for rocket combustion chambers," in Proc. 6th European Conference for Aeronautics and Space Sciences (EUCASS), Kraków, Poland, 2015.

[17] M. Bäker, T. Fiedler, and J. Rösler, "Stress evolution in thermal barrier coatings for rocket engine applications," *Mechanics of Advanced Materials and Modern Processes*, vol. 1, no. 1, pp. 5, 2015.

[18] D. J. Liaw, K. L. Wang, Y. C. Huang, K. R. Lee, J. Y. Lai, and C. S. Ha, "Advanced polyimide materials: Syntheses, physical properties and applications," *Progress in Polymer Science*, vol. 37, pp. 907-974, 2012.

[19] M. E. Clift, "Reverse-buckling rupture disk with replaceable disk and blade," U. S. Patent No. 4,691,729, 8 Sep., 1987.

[20] L. Huang, J. Zhang, X. Song, G. Li, and J. Lai, "The vibration-collision behavior during the diaphragm's fracture in hypersonic impulse facilities," *European Journal of Mechanics-A/Solids*, vol. 109, pp. 105789, 2025.

[21] Q. C. Zhou, J. S. Xu, X. Chen, and C. S. Zhou, "Review of the adhesively bonded interface in a solid rocket

motor," *The Journal of Adhesion*, vol. 92, no. 5, pp. 402-428, 2016.

[22] C. Y. Liao and S. Lee, "Improving bond strength at propellant-liner interfaces," *Journal of Propulsion and Power*, vol. 31, no. 5, pp. 1452-1457, 2015.

[23] B. O. Gercel, D. O. Üner, F. Pekel, and S. Özkar, "Improved adhesive properties and bonding performance of HTPB-based polyurethane elastomer by using aziridine-type bond promoter," *Journal of Applied Polymer Science*, vol. 80, no. 5, pp. 806-814, 2001.

[24] B. Zhang, S. Yuan, R. Ren, Z. Zhang, and Y. Luo, "Influence of the binder structure on the interfacial adhesion and antimigration properties of the propellant charge," *ACS Omega*, vol. 7, no. 7, pp. 6335-6344, 2022.

[25] T. Kitinirunkul, P. Boonyarat, K. Wira, C. Kreemin, T. Boonnok, and A. Namkanisorn, "Effects of accelerated aging and primer on the mechanical properties and bond strength at propellant-liner interfaces," *Chemical Engineering Transactions*, vol. 118, pp. 415-420, 2025.

[26] B. Zhang, S. Yuan, R. Ren, Z. Zhang, and Y. Luo, "Influence of the binder structure on the interfacial adhesion and antimigration properties of the propellant charge," *ACS Omega*, vol. 7, no. 7, pp. 6335-6344, 2022.

[27] J. C. Quagliano Amado, P. G. Ross, L. M. S. Murakami, and J. C. N. Dutra, "Properties of hydroxyl-terminal polybutadiene (HTPB) and its use as a liner and binder for composite propellants: A review of recent advances," *Propellants, Explosives, Pyrotechnics*, vol. 47, no. 5, pp. e202100283, 2022.

[28] ASM International, "ARMCO PH 13-8 Mo stainless steel material property data sheet," in *ASM Aerospace Materials Handbook*, ASM International, 2012.

[29] A. Pai, M. Rodriguez-Millan, C. S. Kumar, C. R. Kini, and S. Shenoy, "Diaphragm rupture dynamics within shock tubes: Experimental and numerical studies of the quatrefoil pattern," *International Journal of Solids and Structures*, vol. 306, pp. 113569, 2025.

[30] C. Wang, C. Chen, Q. Ren, and K. Chen, "Investigation on metal diaphragm of pulse separation device in dual-pulse solid rocket motor," *Proceedings of the Institution of Mechanical Engineers, Part G: Journal of Aerospace Engineering*, vol. 231, no. 3, pp. 444-451, 2017.

[31] X. G. Fan, J. S. Xu, X. Chen, S. X. Wang, and S. Q. Hu, "Investigation on failure properties and constitutive modeling of EPDM used for pulse separation device," *Mechanics of Materials*, vol. 137, pp. 103127, 2019.

[32] H. Hencky, "Uber den spannungszustand in kreisrunden platten mit verschwindender biegungssteifigkeit [On the state of stress in circular plates with vanishing bending stiffness]," *Journal of Mathematics and Physics*, vol. 63, pp. 311-317, 1915.

[33] Y. Li, X. Chen, H. Cheng, and Z. Zhao, "Fluid-structure coupled simulation of ignition transient in a dual pulse motor using overset grid method," *Acta Astronautica*, vol. 183, pp. 211-226, 2021.

[34] W. Cheng, Q. Cao, B. Yuan, and J. Yan, "Experimental and peridynamic numerical study on the opening process of the soft PSD in pulse solid rocket motors," *Computer Modeling in Engineering and Sciences*, vol. 143, no. 3, pp. 3197-3214, 2025.

Appendix A

The objective of this appendix is concise and practical: validate the PSD design across the expected operating envelope (pressure, temperature, and loading rate), quantify burst pressure and opening mode, and verify adhesive/liner integrity and post-Pulse-1 residual strength so analytic TMRM predictions can be tied to measured behavior and shop-floor acceptance. Prior dual-pulse programs and LFK-NG work motivate the staged progression from instrumented component tests to representative motor firings.

A.1 *Test specimens: materials, thicknesses, radii and attachment variants*

Test materials: PH13-8Mo foil, Al7075-T6 foil, Ti-6Al-4V foil, and DuPont™ Kapton® HN film (use manufacturer data for temperature-dependent UTS when sizing). For each material select five thicknesses spanning the expected design range (metals: 0.05, 0.10, 0.25, 0.50, 1.00 mm; Kapton: 25, 50, 75, 100, 125 μm) and at least two port radii (suggest 20 mm and 30 mm or match your motor geometry). For each material/thickness/radius produce unscored controls plus scored variants: four-line radial scribe, concentric ring groove, and cruciform partial cut with three depths (~ 10%, 25%, 50% of thickness). Attachment permutations must include (a) mechanical clamp only, (b) clamp + thin adhesive/sealant bead (use the intended adhesive), and (c) liner/case-bonded specimens where the diaphragm is attached to a cured, treated liner and propellant is cast against that liner. These specimen choices follow the materials, scoring and bonding precedents in the literature and LFK/dual-pulse test programs.

A.2 *Test conditions & instrumentation, staged, high-fidelity measurement*

Static burst tests: run at ambient (~ 25 °C) and elevated temperatures representative of Pulse-1 exposure (suggest 150 °C and 250 °C for polymer limits; include an optional 400 °C metal condition), and at three loading rates (quasi-static ≈ 0.1 MPa/s, moderate ≈ 1 MPa/s, and fast ≈ 10 MPa/s or the fastest achievable to simulate ignition transients). Record high-bandwidth pressure (≥ 100 kHz for fast ramps), high-speed video (≥ 10 k fps if available), acoustic/vibration sensors and systematically collect fragments for post-test forensics; report burst pressure mean & standard deviation, rupture morphology (petal count, fragmentation distribution) and residual tensile strength in the clamp zone. Dynamic/motor-level tests: install candidate PSDs in representative test motors (with insulation and propellant geometry) and perform static firings to Pulse-1 conditions followed by Pulse-2 ignition to verify opening behavior and downstream hardware integrity; repeat each candidate a minimum of three times. Adhesion/liner qualification: execute pull-off (ASTM-style), peel and lap-shear tests on coupon specimens with/without primers (MAPO/BITA/IPDI) and include thermally aged cohorts (e.g., 72 h @80 °C) to quantify bond degradation and validate case-bond vs adhesive options. Instrumentation, post-test sectioning and correlation to residual effective thickness are essential to close the loop with the TMRM.

A.3 *Replication and data practice: statistics for reliability*

Run every combination listed in the specimen matrix (Table 2) with a minimum of three replicates to gather basic statistics (mean, standard deviation, confidence bounds) on burst pressure, opening mode and bond performance (see [22] and [32], [33]); increase replicate counts for near-threshold designs or where variability is large. Record full time-history traces and preserve representative specimens/fragments for metallography, char-depth sectioning and peel/shear coupon testing so statistical burst data can be linked to microscopic damage and interface condition.

A.4 *Success criteria: go/no-go acceptance limits*

The PSD and its attachment must meet these criteria to advance: (1) survive Pulse-1 without rupture at MEOP plus a safety factor (recommended 1.1-1.5) at the test temperature; (2) open reliably under Pulse-2 ignition at the target burst pressure with predictable petalling and minimal fragmentation that does not threaten nozzle integrity; and (3) show no bond line debond, adhesive creep failure, or clamp loss after Pulse-1 (liners/primers must retain peel/shear margins post-aging). Designs that fail any criterion require iteration of material, scoring depth/pattern, thermal backing or bonding workflow prior to motor-level qualification.

Table 2. Test matrix (sample, condensed view)

ID	Material	Thickness	Radius	Scoring	Attachment	Temp (°C)	Loading rate
M1	Kapton HN	50 µm	30 mm	None	Clamp + Liner	25	0.1 MPa/s
M2	Kapton HN	50 µm	30 mm	Radial 4 × 10%	Clamp + Liner	200	1 MPa/s
M3	PH13-8Mo	0.1 mm	30 mm	Ring 25%	Clamp	25	0.1 MPa/s
M4	PH13-8Mo	0.1 mm	30 mm	Ring 25%	Clamp	400	1 MPa/s
M5	Al7075-T6	0.25 mm	20 mm	Radial 4 × 25%	Clamp + Adh	250	10 MPa/s
...	...	...	...	...	...	...	...